

Lawrence Berkeley National Laboratory

LBL Publications

Title

Prospects for the expansion of standing wave ambient pressure photoemission spectroscopy to reactions at elevated temperatures

Permalink

<https://escholarship.org/uc/item/6m15m7qh>

Journal

Journal of Vacuum Science & Technology A Vacuum Surfaces and Films, 40(1)

ISSN

0734-2101

Authors

Karslıoğlu, Osman
Trotochaud, Lena
Salmassi, Farhad
[et al.](#)

Publication Date

2022

DOI

10.1116/6.0001353

Peer reviewed

Prospects for the expansion of standing wave ambient pressure photoemission spectroscopy to reactions at elevated temperatures

Cite as: J. Vac. Sci. Technol. A 40, 013207 (2022); <https://doi.org/10.1116/6.0001353>

Submitted: 12 August 2021 • Accepted: 25 October 2021 • Published Online: 03 December 2021

 Osman Karslıoğlu,  Lena Trotochaud, Farhad Salmassi, et al.

COLLECTIONS

Paper published as part of the special topic on [Commemorating the Career of Charles S. Fadley](#)



View Online



Export Citation



CrossMark

ARTICLES YOU MAY BE INTERESTED IN

Hard x-ray photoelectron spectroscopy of tunable oxide interfaces


Journal of Vacuum Science & Technology A 40, 013215 (2022); <https://doi.org/10.1116/6.0001491>

Searching for superconductivity in high entropy oxide Ruddlesden–Popper cuprate films


Journal of Vacuum Science & Technology A 40, 013404 (2022); <https://doi.org/10.1116/6.0001441>

Engineering ordered arrangements of oxygen vacancies at the surface of superconducting La₂CuO₄ thin films

Journal of Vacuum Science & Technology A 40, 013214 (2022); <https://doi.org/10.1116/6.0001473>



HIDEN
ANALYTICAL




Instruments for Advanced Science

- Knowledge,
- Experience,
- Expertise

Click to view our product catalogue


Contact Hiden Analytical for further details:
www.HidenAnalytical.com
info@hideninc.com

Gas Analysis




- ▶ dynamic measurement of reaction gas streams
- ▶ catalysis and thermal analysis
- ▶ molecular beam studies
- ▶ dissolved species probes
- ▶ fermentation, environmental and ecological studies

Surface Science




- ▶ UHVTPD
- ▶ SIMS
- ▶ end point detection in ion beam etch
- ▶ elemental imaging - surface mapping

Plasma Diagnostics



- ▶ plasma source characterization
- ▶ etch and deposition process reaction kinetic studies
- ▶ analysis of neutral and radical species

Vacuum Analysis



- ▶ partial pressure measurement and control of process gases
- ▶ reactive sputter process control
- ▶ vacuum diagnostics
- ▶ vacuum coating process monitoring

Prospects for the expansion of standing wave ambient pressure photoemission spectroscopy to reactions at elevated temperatures

Cite as: J. Vac. Sci. Technol. A 40, 013207 (2022); doi: 10.1116/6.0001353

Submitted: 12 August 2021 · Accepted: 25 October 2021 ·

Published Online: 3 December 2021



Osman Karslıoğlu,¹ Lena Trotochaud,² Farhad Salmassi,³ Eric M. Gullikson,³ Andrey Shavorskiy,⁴ Slavomir Nemšák,^{5,a)} and Hendrik Bluhm^{1,5,6,a)}

AFFILIATIONS

¹Chemical Sciences Division, Lawrence Berkeley National Laboratory, Berkeley, California 94720

²Center for WaSH-AID, Duke University, Durham, North Carolina 27701

³Center for X-Ray Optics, Lawrence Berkeley National Laboratory, Berkeley, California 94720

⁴MAX IV Laboratory, Lund University, P.O. Box 118, SE-221 00 Lund, Sweden

⁵Advanced Light Source, Lawrence Berkeley National Laboratory, Berkeley, California 94720

⁶Fritz Haber Institute of the Max Planck Society, Faradayweg 4-6, D-14195 Berlin, Germany

Note: This paper is a part of the Special Collection Commemorating the Career of Charles S. Fadley.

a) Authors to whom correspondence should be addressed: snemsak@lbl.gov and bluhm@fhi-berlin.mpg.de

ABSTRACT

Standing wave ambient pressure photoemission spectroscopy (SWAPPS) is a promising method to investigate chemical and potential gradients across solid-vapor and solid-liquid interfaces under close-to-realistic environmental conditions, far away from high vacuum. Until now, these investigations have been performed only near room temperature, but for a wide range of interfacial processes, chief among them being heterogeneous catalysis, measurements at elevated temperatures are required. One concern in these investigations is the temperature stability of the multilayer mirrors, which generate the standing wave field. At elevated temperatures, degradation of the multilayer mirror due to, for example, interdiffusion between the adjacent layers, decreases the modulation of the standing wave field, thus rendering SWAPPS experiments much harder to perform. Here, we show that multilayer mirrors consisting of alternate B₄C and W layers are stable at temperatures exceeding 600 °C and are, thus, promising candidates for future studies of surface and subsurface species in heterogeneous catalytic reactions using SWAPPS.

© 2021 Author(s). All article content, except where otherwise noted, is licensed under a Creative Commons Attribution (CC BY) license (<http://creativecommons.org/licenses/by/4.0/>). <https://doi.org/10.1116/6.0001353>

I. INTRODUCTION

Interfaces govern many important processes in the environment and technology. While they can be vastly different in character, e.g., ranging from solid-solid to solid-liquid to solid-vapor, they share the basic characteristic of a discontinuity across the interface in the chemical composition, density, structure, as well as chemical and electrical potentials. Interfaces play a central role in a wide range of technological and environmental phenomena, such as cloud formation,¹ the production of important chemicals such as ammonia,² the leaching of toxic substances from mining waste,³ and the corrosion of metals.⁴ For a fundamental understanding of the interface on the atomic scale, it is essential that the chemical

composition and other properties of the interface and the adjacent bulk phases are investigated with high spatial resolution in the direction across the interface, as well as in-plane.

There are a number of different approaches to the investigation of interfaces with high spatial (angstroms to nanometers) resolution in the direction normal to the interface. Among them are cross-sectional transmission and scanning electron microscopy^{5,6} as well as scanning transmission x-ray microscopy.⁷ These techniques provide information on the atomic positions not only in the direction across the interface, but also in the plane of the interface. A downside of these methods is the necessary preparation of the cross section for examination.^{8,9} An example for a nondestructive

method is surface x-ray diffraction,¹⁰ which, however, lacks information on local variations in the interface properties and averages over the whole probed volume.

X-ray photoelectron spectroscopy (XPS)¹¹ has been a standard method for the investigation of interfaces for decades due to its intrinsic surface and chemical sensitivity and nondestructive nature. The strong interaction of electrons with matter enables depth profile measurements at the solid–vapor or liquid–vapor interfaces through a variation of the electron kinetic energy or emission angle, since surface electrons are less scattered than those originating from deeper in the bulk. The resulting measurements are, however, often ambiguous, due to the convolution between the dependence of the photoelectron intensity as a function of depth and the actual chemical or potential depth profile of interest. Another challenge specific to buried interfaces is the competition between the weak signal from the narrow interfacial region with the signal from the bulk phases on either side of the interface. Thus, depth profiling with XPS is always highly dependent on the quality of assumptions and models about the depth distribution of chemical species or potentials, i.e., the very quantity that generates interest in Ref. 12.

These problems can be tackled through the generation of a standing x-ray wave field with a known wavelength in the direction perpendicular to the interface.¹³ The standing wave is generated by scattering the x rays under the Bragg condition in the sample substrate. X rays are scattered by the lattice planes of a single crystal or by the interfaces of a multilayer mirror (MLM) substrate with a periodicity that can be adjusted to the available x-ray wavelengths, usually in the range of a few to several nanometers. The relative position of the standing wave with respect to the interface is varied by tuning the incidence angle or the energy of the x rays through the first (or higher) order Bragg angle, resulting in a shift of the position of the standing wave nodes and antinodes by roughly half of the standing wave period.

Interface-sensitive measurements using standing waves have been performed for many decades using, e.g., fluorescence yield detection^{14,15} at the solid–liquid interfaces, revealing the relative positions of ions in solution with respect to the interface. Fadley and co-workers recognized the opportunities that the combination of the standing wave technique with XPS provides for the investigation of interfaces, especially buried ones, with high chemical and spatial sensitivity and carried out the first experiments using this method.^{16,17} The main upside of this combination of methods is that the known periodicity of the x-ray standing wave provides an intrinsic “ruler” in the direction perpendicular to the interface. This ruler overcomes the uncertainties in the value for the electron mean free path and, thus, increases the spatial resolution in the direction perpendicular to the interface to the sub-nanometer scale.

The expansion of standing wave XPS into the domain of *in situ* and *operando* techniques became possible via its combination with ambient pressure XPS (APXPS).^{18,19} APXPS has now become a routine method for the investigation of surfaces under realistic conditions,^{20–22} which is important in areas as diverse as environmental science, electrochemistry, and heterogeneous catalysis. Some of the important questions in these experiments are the role of subsurface species in heterogeneous interfacial reactions as well

as chemical and potential gradients across the interface under reaction conditions. Standing wave ambient pressure photoemission spectroscopy (SWAPPS) was established to probe the interface compositional and potential gradients with high spatial resolution. This method was first used to investigate the relative position of hydrated cesium and sodium ions with respect to a hematite/water vapor interface.²³ SWAPPS was also employed to study the corrosion of Ni in the presence of a KOH solution.²⁴ In both cases, the samples of interest, FeO_x and Ni, were grown on a multilayer mirror (MLM) to match the energy range of the x-ray sources (beamlines 11.0.2. and 6.0.1 at the Advanced Light Source in Berkeley, CA) to achieve the formation of a standing wave. Both experiments were carried out near room temperature to maintain a stable solid–liquid interface.

One area of research where SWAPPS could address important research questions, such as the distribution of subsurface species, is heterogeneous catalysis, which in the overwhelming number of relevant reactions, requires elevated temperatures. So far, the limited number of SWAPPS measurements have been performed only at room temperature. For heterogeneous catalysis, the most important interface is that of a gas with a solid, which can be evaluated using soft x rays and electron kinetic energies below 1 keV for moderate pressures in the mbar range. Under these conditions, the generation of standing waves using multilayer mirrors is preferential to that of using the natural lattice spacing in single crystals since the standing wave period of several nanometers matches the typical width of interfacial regions.

Artificial multilayers with periodicities in the nm range are commonly utilized as mirrors for soft x-ray instruments and in EUV lithography, where they are exposed to high radiation and heat load. The performance of an MLM depends strongly on factors such as interface roughness and interdiffusion between layers, which may be affected adversely by changes in temperature. For investigations of chemical changes at surfaces at elevated temperatures, MLMs with high thermal stability are, thus, required. A material combination that is known to be stable at relatively high temperatures is B₄C and W.²⁵ The thermal stability of B₄C/W MLMs has been characterized by techniques that are sensitive to physical properties such as layer thickness, interface roughness, and crystallinity.^{26–29} Since the current applications of these mirrors rely mainly on their physical properties, the chemical properties of the surface have not been the main focus of investigations so far. For studies of interfacial chemistry, such as in the area of heterogeneous catalysis, a thorough characterization of the chemical properties of these MLMs under elevated temperatures is required.

The purpose of this work is to explore the applicability of B₄C/W MLMs to heterogeneous catalytic reactions at elevated temperatures. In particular, we studied the surface properties of B₄C/W MLMs as a function of annealing temperature in UHV using x-ray photoelectron spectroscopy (XPS) with synchrotron radiation. Our results demonstrate that the first few nanometers of the surface (B₄C-termination) are partially oxidized. In addition, we show that, in agreement with previous studies, the ML mirror quality is preserved at least up to 700 °C, which is more than sufficient to generate a usable standing wave pattern for SWAPPS experiments of model heterogeneous catalysts under realistic thermal conditions.

II. EXPERIMENT

The B₄C/W multilayers were prepared by magnetron sputtering on a 4-in. Si(100) substrate by the Center for X-ray Optics at Lawrence Berkeley National Laboratory (sample No. CX150831B). The fabrication parameters were set to a period of 3.38 nm, 60 bilayer repeats, and a W-thickness ratio of 32%, i.e., the nominal thickness of each W layer was 1.08 nm and that of each B₄C layer was 2.30 nm. The termination layer was B₄C. The samples were stored in air before the XPS measurements.

The XPS measurements were performed at beamline 11.0.2 of the Advanced Light Source³⁰ at the Lawrence Berkeley National Laboratory using the APXPS-1 endstation.¹⁹ The vacuum chamber had a base pressure of better than 1×10^{-8} mbar. A small sample of approximately 1 cm² in size was cut from the MLM wafer and used for the measurements. The sample was mounted on a commercial alumina encapsulated button heater (HeatWave Labs) which can be operated in an atmosphere of 1 mbar O₂ at temperatures of up to 1000 °C. The sample was affixed to the holder by two stainless-steel clips. Under the clips, small alumina pieces were placed for electrical isolation. A K-type thermocouple wire was placed under one of the alumina pieces, in contact with the surface of the sample. The thermocouple was used both for temperature measurements and for measuring the sample current resulting from photoemission. The sample current was used to calibrate the Bragg angle in the standing wave measurements, which were performed by changing the incident angle of the x rays on the sample using a rotational stage on the sample manipulator. The sample was oriented with its normal in the plane of the synchrotron.

The multilayer sample was measured in vacuum at room temperature and afterward heated from 300 °C to 700 °C in 100 °C steps to test its thermal stability. It was kept at each target temperature for 15 min before cooling down and acquiring the XPS spectra near room temperature.

The binding energy (BE) scale was calibrated using the Fermi edge ($E_b = 0$). The combined beamline/analyzer resolution was better than 0.35 eV. For spectra acquired around 200 eV electron kinetic energy (KE), a transmission-function correction was

applied, which was a linear function of KE. This was necessary due to the significant loss of intensity at lower kinetic energies. The correction function was obtained as an average from survey spectra taken with 850 and 880 eV photon energies, which had flat backgrounds in that region.

The electron spectrometer was mounted under the magic angle (54.7°) with respect to the incident photon beam. The rocking curves in the standing wave experiments were taken around the first order Bragg angle (12.5° grazing incidence) at an incident photon energy of 850 eV. The XPS spectra for the characterization of the surface chemistry were taken around 14° grazing incidence. The detection angle in the XPS measurements between sample normal and photoelectron spectrometer was, thus, about 45°. The approximate probing depths for electrons with a given KE are reported as three times the inelastic mean free path (λ) in pure boron, as calculated by the TPP-2M formula, and under consideration of the detection angle.³¹ The XPS data were analyzed using the KolXPD software.³² Simulations of electric field strength and photoemission signal intensity as a function of incidence angle (so-called rocking curves) were performed using the YXRO software.³³ Only W 4f and B 1s spectra were collected for standing-wave analysis.

III. RESULTS AND DISCUSSION

We first discuss the core level spectra and their evolution as a function of temperature before turning our attention to the standing wave properties of the MLMs. These measurements provide information on the stability of the MLMs at elevated temperatures.

A. Analysis of the surface chemistry from XPS

XPS measurements of the surface composition of the as-prepared B₄C/W MLM were performed at a constant KE of 200 eV to maintain the same probing depth for all core levels. The termination layer in our MLM is B₄C with an expected thickness of 2.3 nm. The probing depth for 200 eV KE electrons in the present experimental geometry is approximately 1.8 nm, which means that

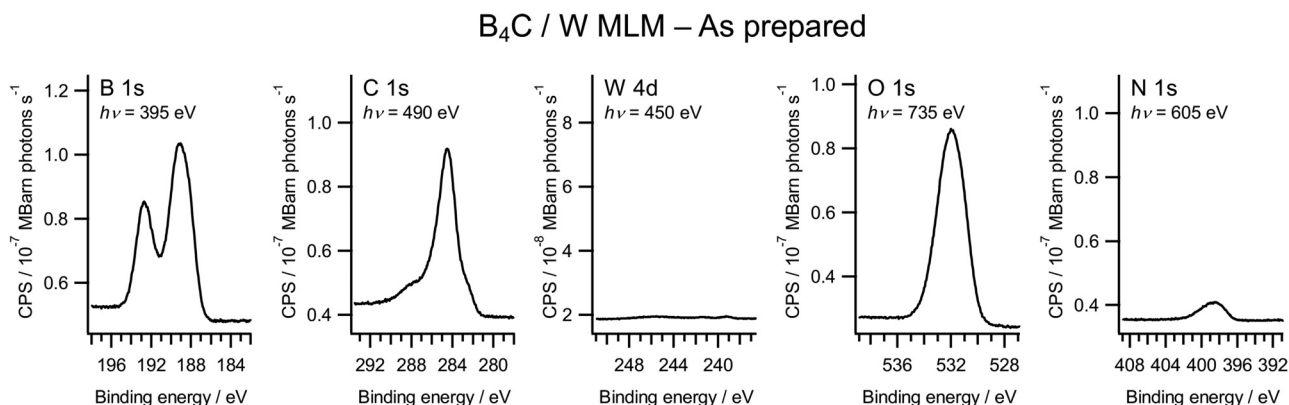


FIG. 1. Core-level spectra from the as-prepared B₄C/W MLM sample in the B 1s, C 1s, W 4d, O 1s, and N 1s regions. In all cases, the photoelectron kinetic energies are in the range of 200 eV to have the same probing depth for all the elements. The y axes cover the same cps range to allow for a direct comparison of peak heights.

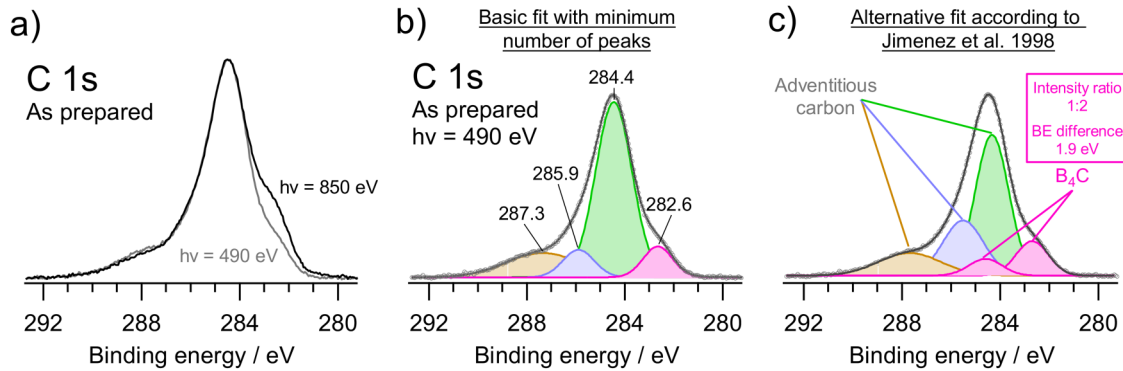


FIG. 2. C 1s spectra of the as-prepared MLM: (a) at photon energies of 490 and 850 eV, with the spectra normalized to their maximum intensity after the subtraction of a Shirley background. (b) Peak fitting analysis for the spectrum taken at a photon energy of 490 eV using the minimum necessary number of peaks, and (c) using the constraints put forward by Jimenez *et al.* in Ref. 34, i.e., a 1:2 intensity ratio and 1.9 eV BE difference for the B₄C-related C 1s peaks in the low-BE region.

the signal is expected to originate almost exclusively from the B₄C layer. B 1s, C 1s, W 4d, O 1s, and N 1s spectra from the as-prepared state of the sample are shown in Fig. 1. In addition to boron and carbon, which were deposited during preparation, there is also oxygen and nitrogen on the surface. The oxygen component originates most likely from the oxidation of boron during the storage of the MLM in air prior to the measurements. The source

for the presence of nitrogen at the surface is unclear, and possible causes are contact with N-containing organic contaminants during transfer through air or impurities in the sputtering target during deposition. Some W is also observed. The low intensity of W in the W 4d spectrum suggests that it is indeed buried under the B₄C layer and has not diffused out significantly.

Figure 2(a) shows the C 1s spectra from the as-prepared sample, taken with 490 and 850 eV photon energies, which correspond to ~200 and ~560 eV KE, and probing depths of ~1.8 and ~3.4 nm, respectively. The main difference between the spectra is the component at the lowest BE, which is stronger for the spectrum taken at the higher photon energy. This indicates that the corresponding chemical species is located deeper in the sample than in the other C species. The peak fitting analysis [Fig. 2(b), basic fit with a minimum number of peaks] reveals a BE of 282.6 eV for this component, consistent with C in B₄C, as reported earlier by Yang *et al.* for a similar MLM.^{35,36} For an oxide-free B₄C surface, Jimenez *et al.* reported two C 1s peaks at 281.8 and 283.7 eV with an intensity ratio of 2:1, respectively, corresponding to C in a CBC chain (281.8 eV) and in an icosahedral motif (283.7 eV) in the B₄C structure.³⁴ It is likely that the same two peaks are present in our spectrum at 282.6 and 284.5 eV, with the 284.5 eV peak overlapping with the peak at 284.4 eV, which we associate with adventitious carbon. Using this information, we add another peak into the fitting at 1.9 eV higher BE with respect to the lowest BE peak, with the corresponding 2:1 intensity ratio. The result is shown in Fig. 2(c) as an alternative fit. This analysis indicates that most of the C 1s signal originates from adventitious carbon.

The B 1s spectra from the as-prepared sample are displayed in Fig. 3. In Fig. 3(a), B 1s spectra taken with 395 and 850 eV photon energy are shown. These correspond to electron KEs of ~200 and ~655 eV, and probing depths of ~1.8 and ~3.8 nm, respectively, comparable with the values used for the C 1s spectra. The main difference between the two spectra is observed in the shape and position of the low BE feature at around 189 eV, which is ascribed to B in B₄C.³⁴ The peak fitting analysis [Fig. 3(b)] indicates that the low BE side of the signal can be fit with two peaks, one at 189.5 eV and the other at 188.4 eV. The intensity of the 189.5 eV peak relative to

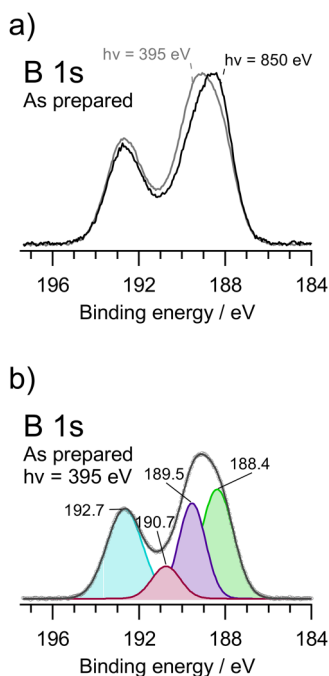


FIG. 3. B 1s spectra of the as-prepared MLM: (a) at photon energies of 395 and 850 eV. The spectra are normalized to their maximum intensity after the subtraction of a Shirley background. (b) Peak fitting analysis for the spectrum taken at a photon energy of 395 eV.

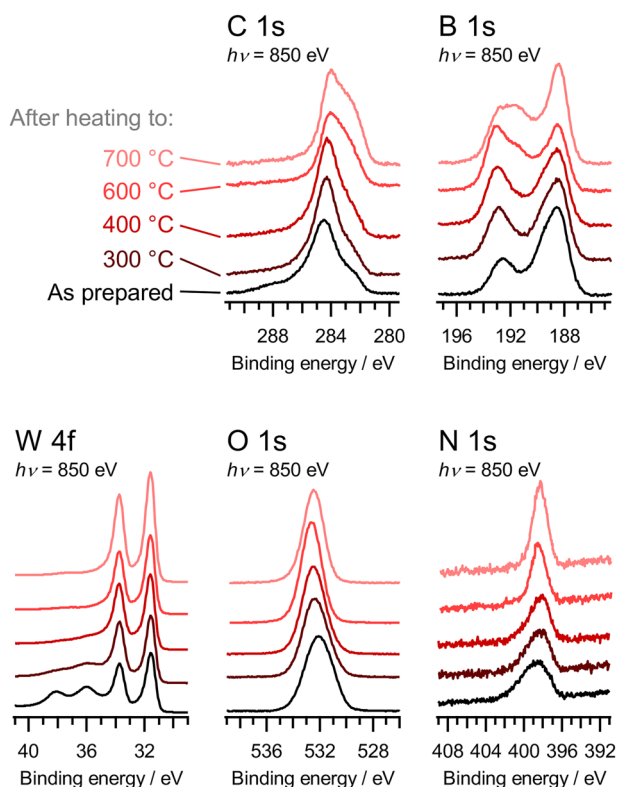


FIG. 4. Spectra after heating to increasingly higher temperatures, with the spectra acquired after cooling down to near room temperature. B 1s, C 1s, and O 1s spectra are displayed after a Shirley-background subtraction. The spectra are offset along the y axis for clarity.

that of the 188.4 eV peak increases with increasing photon energy, indicating that the 188.4 eV component is on average located deeper than the 189.5 eV component. The peak at 192.7 eV is likely due to B_2O_3 , based on its binding energy and the significant amount of oxygen observed in the O 1s region. The 190.7 eV component might originate from B^{2+} species, which probably would have oxygen coordination.³⁴ Another interpretation of this component is that it is due to a B–N compound such as BN. The supporting evidence for this interpretation is the observed BE difference between this B 1s component (190.7 eV) and the N 1s peak (~ 398.5 eV) being in the range of the reported values for BN in the literature (207.5–207.8 eV). The intensity expected for the B 1s component based on the N 1s intensity and the photoemission cross sections of the two core levels yields a consistent fit for the heating series. Therefore, we follow this interpretation for our analysis.

We now turn our attention to the discussion of the core level spectra as a function of temperature. Figure 4 shows C 1s, B 1s, W 4f, O 1s, and N 1s spectra after each heating step. The initial W 4f spectrum shows two main doublets, with the $4f_{7/2}$ components at 31.45 and 36.0 eV, which we assign to metallic W and WO_3 , respectively.³⁷ The presence of WO_3 is probably the result of exposure to

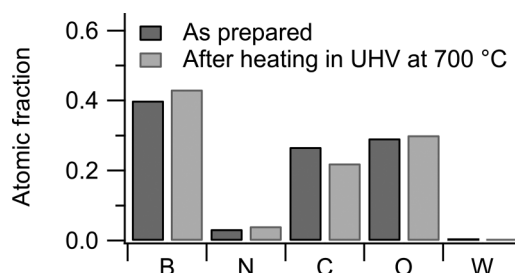


FIG. 5. Surface composition of the B_4C/W MLM, as prepared and after annealing at 700 °C in UHV. All core levels were measured with 200 eV KE, thus the probing depth is ~ 2.5 nm.

air. Based on the very low signal in the W 4d region (see Fig. 1), WO_3 is not expected to be on the surface, but rather at the B_4C/W interface. This means the oxidation of W took place via the diffusion of oxygen through the B_4C layer. The WO_3 component decreases with each heating step and is mostly gone after heating to 600 °C. Similarly, the O 1s spectrum loses intensity on the low BE side (WO_3 , O 1s ~ 531 eV) and gains intensity on the high BE side (B_2O_3 , O 1s ~ 532.5 eV). This suggests that WO_3 reacts with B_4C to form W and BO_x , which also explains the increase in the ~ 192.7 eV B 1s signal. This will be shown in more detail below in the peak fitting analysis of the B 1s and O 1s regions.

The compositions of the as-prepared MLM surface and the surface after the last heating step at 700 °C are shown in Fig. 5. The core levels B 1s, C 1s, N 1s, O 1s, and W 4d have been measured with different photon energies that correspond to 200 eV KE, which translates to a probing depth of ~ 2.5 nm. For calculating the atomic fractions, a homogeneous mixture through the probing depth was assumed and the intensities were normalized for photon flux and photoemission cross sections. Even though there is no drastic change in composition, a decrease in carbon fraction from 0.27 to 0.22 is observed along with an increase in the fractions of other elements, which can be explained by the desorption of some adventitious carbon from the surface. It is indeed clear that the C 1s intensity above ~ 286 eV diminishes already after heating to 300 °C (Fig. 4). The oxygen fraction does not decrease—in fact it increases slightly—consistent with an earlier work on the thermal stability of the oxides on B_4C where the O 1s signal disappears at ~ 1230 °C.³⁴

Peak-fitted B 1s spectra for the heating series are shown in Fig. 6(a). The fitted components are labeled B_A to B_E from low to high BE. The fraction and intensity of each component is plotted as a function of treatment in Figs. 6(b) and 6(c), respectively.

The reported B 1s binding energies in the literature for fully oxidized boron compounds such as B_2O_3 and H_3BO_3 are typically in the range of 192.4–193.5 eV.^{34–42} The B 1s–O 1s peak separation in these compounds, which is independent of sample charging, is ~ 339.7 eV.^{42–44} Since H_3BO_3 decomposes to B_2O_3 and H_2O at 330 °C,⁴⁵ we assume that the B_E peak is solely due to B_2O_3 , at least after heating at 400 °C. B_2O_2 has a B 1s BE that is ~ 1 eV lower than that of B_2O_3 and a B 1s–O 1s peak separation of ~ 340.7 eV.^{46,47} Lower oxidation states of boron (B^{+x} , $0 < x < 1$) in

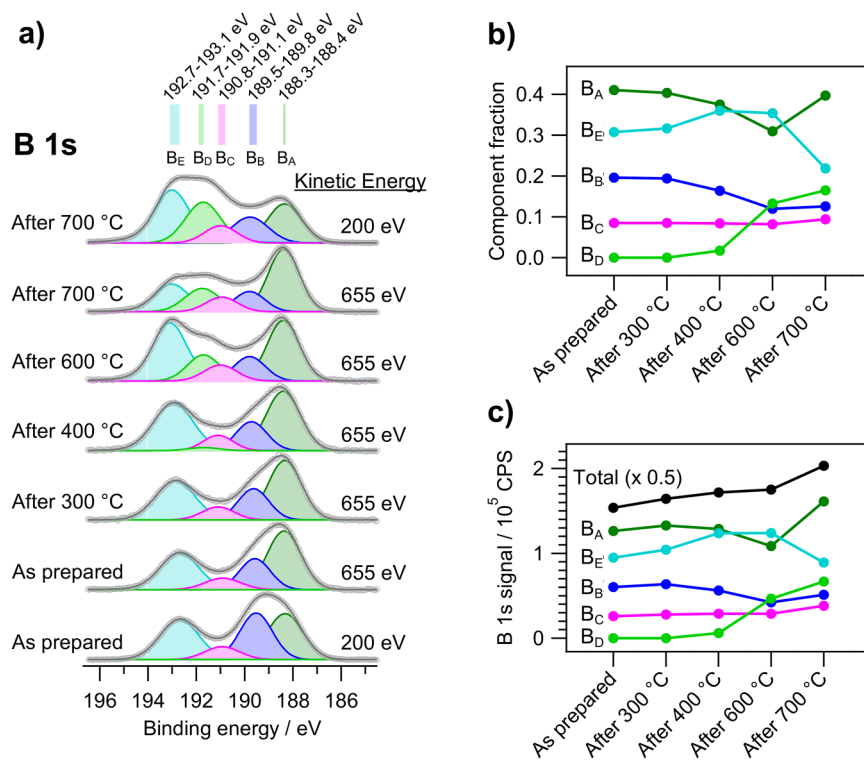


FIG. 6. Peak fitting analysis of the B 1s region: (a) B 1s spectra for the B₄C/W MLM, as prepared and after heating in UHV to increasing temperatures. The spectra are fit with five components, denoted B_A–B_E. Fractions (b) and intensities (c) of the components B_A–B_E after each treatment.

binary boron oxides are reported to have significantly lower BEs, in the range of 188–189 eV.^{39,41} In light of these information, we can assign peaks B_E and B_D to B₂O₃ and B₂O₂, respectively. As we will discuss in the following paragraphs, the total oxygen content of the sample does not change appreciably after the heating treatments. This leads us to postulate that B in B₄C acts as a reducing agent in the formation of B₂O₂ via the reaction $2B_2O_3 + 2B \rightarrow 3B_2O_2$.

The peak fitting analysis of the O 1s region is shown in Fig. 7(a). From the W 4f, C 1s, and B 1s spectra, we already expect to see signatures of WO₃, –CO_x, and B₂O₃. In addition, a small peak above 533 eV is necessary to account for the intensity in that region. Thus, the broad O 1s envelope is best fitted with four peaks. From values in the literature for W 4f–O 1s and B 1s–O 1s peak separations, O_A (WO₃) and O_C (B₂O₃) can be placed at 530.8 eV and ~532.5 eV, respectively.^{42,48} We do not attempt to perform a rigorous analysis of the contribution of carbonaceous contamination to the O 1s spectrum; however, a peak around 531.4 eV (O_B) is used to account for at least some of the oxygen that originates from this source. The origin of O_D is not immediately clear. If we assign the B_D peak to B₂O₂, the corresponding O 1s peak would be at ~532.5 eV,^{46,47} which overlaps with O_C. If O_D is assigned to B₆O, the corresponding B 1s peaks would appear at 189.2/187.4 eV,^{39,49} which is inconsistent with the observed B 1s spectra. An alternative explanation is that O_D is the energy loss feature of O_C. The loss energy, which is estimated to be ~0.9 eV, is consistent with the reported bandgap values for B₄C (0.77–1.80 eV, depending on carbon content) and boron (0.88–1.6 eV, depending on factors such as crystal quality and purity).^{50–57}

In Fig. 7(b), the intensities after each treatment are given for the four O 1s components and their sum total. The total O 1s signal changes very little, about –10% between the as-prepared to the sample annealed at 700 °C, which indicates that the changes in the intensities of the individual components are mainly due to the transfer of oxygen from one compound (WO₃) to the other (B₄C).

B. Standing-wave analysis

The four components that make up the B 1s spectrum can be further analyzed via x-ray standing-wave photoemission. We first consider the calculated electric field map generated by the MLM under investigation, shown in Fig. 8. The electric field map was calculated assuming nominal growth thicknesses of the respective mirror layers, B₄C termination, no interdiffusion between the B₄C and the W layers, and perfectly flat interfaces. Although we know that the actual roughness/interdiffusion between the layers, for a qualitative analysis this a good approximation. Horizontal cuts of the electric field map at certain depths, which correspond to the calculated rocking curves, are shown as traces to the right of the 2D map in Fig. 8 and demonstrate how the measured rocking curves are expected to change as the standing wave field moves vertically through the MLM. The calculated rocking curve inside the W region shows first a minimum and then a maximum with increasing angle. As we move into the B₄C termination layer and toward the surface, the incidence angle at which the maximum intensity is observed shifts to lower values. We will use the calculations shown

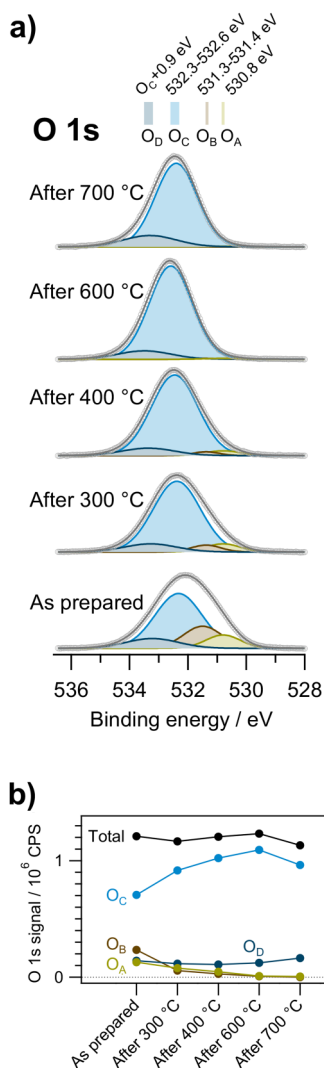


FIG. 7. Peak fitting analysis of the O 1s region: (a) O 1s spectra for the B₄C/W MLM, as prepared and after heating in UHV to increasing temperatures. The spectra are fitted with four components, denoted O_A–O_D. Photon energy is 850 eV. (b) Fractions of the components O_A–O_D after each treatment.

in Fig. 8 to determine the ordering of the species with respect to the vacuum interface that give rise to the four peaks in the B 1s spectrum.

Figure 9 shows the core-level intensity profiles as a function of incidence angle (i.e., the rocking curves) for the B 1s components B_A–B_E and the W 4f components W and WO₃. Based on the peak positions from the as-prepared sample, the relative depths of the species are in the order (from deepest to shallowest): W → WO₃ → B_A → B_B. The presence of WO₃ in between B and W indicates the diffusion of oxygen to the B₄C/W interface, as opposed to diffusion of W to the surface. This also suggests that oxidized boron is likely

present throughout the B₄C layer. The peak position of B_B in the rocking curve is always at lower incidence angles than that of B_A, indicating that B_A is nearer to W than B_B. The B_C signal is relatively weak, and, therefore, small differences in peak fitting may change the shape of its rocking curve considerably. It is, thus, difficult to draw a strong conclusion about the B_C location based on the position of the rocking curve maximum. The B_D signal increases considerably at high temperatures so that a reliable rocking curve for this species can be obtained after annealing to 600 °C and above. Based on its rocking curve peak shape, B_D is nearer to the surface than B_A or B_B. For the as-prepared sample, the B_E intensity shows a sloping background and no clear maximum. Earlier, we assigned B_E to B₂O₃, and the slope in the rocking curve of the as-prepared sample (which is measured from high to low angles) might be a temporal effect and the result of x-ray beam-induced oxidation of B₄C by residual H₂O (or possibly O₂) in the chamber. This change in the B₂O₃ thickness during the acquisition of the rocking curves may explain the weak standing wave effect, in addition to a broad distribution of oxygen within the B₄C layer. After 700 °C annealing, the rocking curves of B_C, B_D, and B_E become very similar, with identical peak positions at a lower angle than B_A and B_B, indicating the formation of a mixed layer containing B, O, and N on the surface. The rocking curve amplitude of B_B increases after annealing at 600 °C, concomitant with a decrease in the XPS intensity of the B_B component. Both trends are consistent with a thinning of the B_B layer. A reverse trend is observed after annealing at 700 °C. A similar trend can also be observed for the intensity of the B_A component [Fig. 6(b)], but its rocking curve amplitude remains relatively unchanged (Fig. 9). This suggests that the B_A and B_B species are spatially distributed in a relatively similar volume. Additionally, judging by the slight change in the position of the RC maxima, on average, both B_B and B_A components appear to migrate toward the surface during the annealing process.

The peak-to-peak amplitude of the W rocking curves (lower traces in Fig. 9) decreases significantly after annealing to 500 °C but remains approximately constant between 500 and 700 °C. This is in line with the reduction of WO₃ to W, which should increase the thickness of the W layer, resulting in a smaller peak-to-peak amplitude. The shape of the W rocking curve changes only slightly between 500 and 700 °C, indicating only minimal changes in the position of the topmost W layer with respect to the periodic interfaces.

To provide more quantitative information on the morphological changes during the annealing process, we used the same nominal definition of the superlattice as for the electric field strength calculations (Fig. 8) and simulated the influence of the interdiffusion between W and B₄C layers on the shape of the photoemission rocking curves. Figure 10 shows a series of simulations of total B 1s and W 4f intensities as a function of incidence angle, assuming linear interdiffusion profile with increasing length between 0.0 and 1.0 nm.

For perfectly flat interfaces with no interdiffusion, the calculated rocking curve modulation (maximum–minimum, normalized to 1 at an off-Bragg angle) is ~80% for W 4f and ~60% for B 1s. This difference in modulation is caused by the different thicknesses of the W and B₄C layers (W is nominally only half as thick as

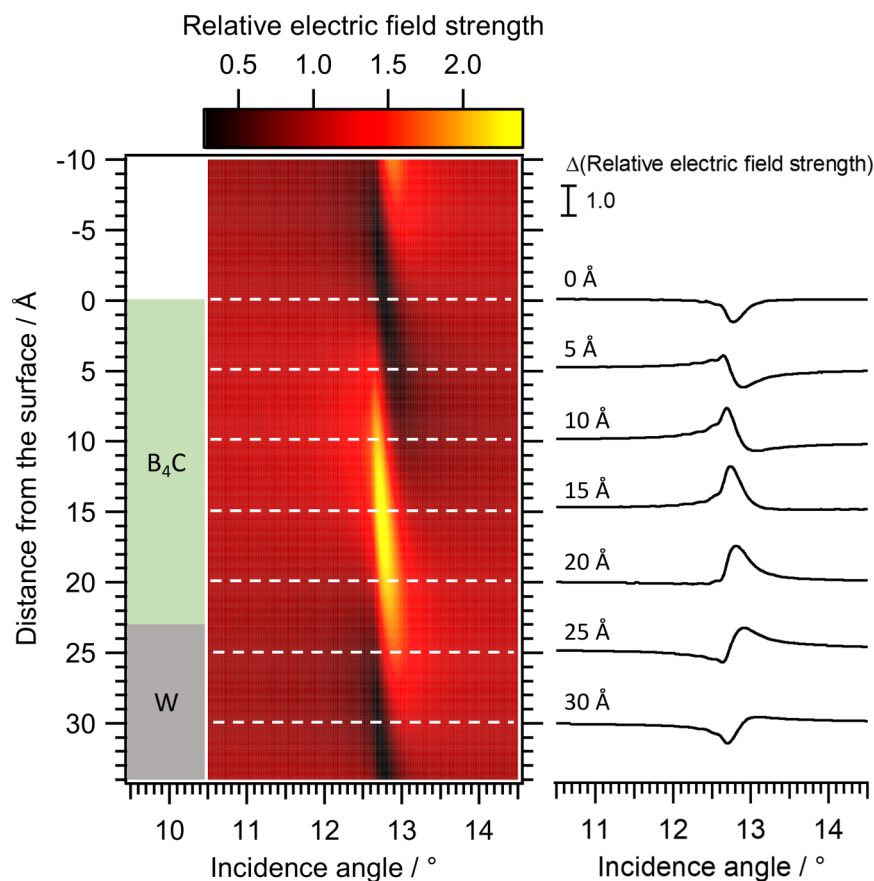


FIG. 8. Calculated electric-field map within the top B₄C/W layers (left) and slices of the map taken at 0, 5, 10, 15, 20, 25, and 30 Å depth into the sample (right). The calculation was performed using the YXRO package assuming no interdiffusion/roughness between the layers of the MLM.

B₄C). With increasing interdiffusion, the SW modulation for W 4f gradually decreases to ~60% at 0.6 nm and ~40% at 1.0 nm. The B 1s rocking curves follow the same trend, with the SW modulation dropping to ~40% at 1 nm interdiffusion. Based on a comparison of the simulated (Fig. 10) and the experimental data of the W 4f rocking curves modulation (Fig. 9), one can conclude that the interdiffusion between W and B₄C layers in our sample increased from ~0.6 to 0.8 nm when annealing the “as-prepared” sample to 700 °C. In this case, rocking curve amplitude analysis serves as a sufficient approximate quantification, since one can conclude that even at high temperatures, the multilayer produces a sufficiently strong standing wave (as demonstrated by strong modulations of B 1s and W 4f rocking curves). The full analysis that also compares shapes and position of the rocking curves maxima and minima would yield more precise results, however, for the cost of much heavier computational efforts.

The results of the rocking curve and photoemission data analysis are summarized in Fig. 11, where the left panel represents the ideal MLM structure right after growth (not measured by us), and the middle and right panel denote the sample structure as determined from our experiments, both before (as-prepared) and after the heating cycles, respectively. It is obvious that the top layer of a W/B₄C MLM is to a large degree oxidized, including the buried W top layer. This needs to be kept in mind when further layers are

grown as samples of interest on top of the MLM. Based on these findings, it is clear that O diffusion through the B₄C layer is a significant issue that has to be taken into consideration for catalysis studies with these MLMs. For example, studying the catalytic properties of an oxide layer grown on a B₄C-terminated MLM is likely to suffer from diffusion of oxygen into B₄C at temperatures exceeding 300 °C, complicating the interpretation of the results, and possibly affecting the performance of the MLM. To circumvent this problem, a barrier layer can be prepared between the sample layer and B₄C, which could, in principle, prevent oxygen diffusion and protect the MLM. An example to this approach was shown to be feasible for preventing V and Ti diffusion through TiO₂ by using a Ta + TiO₂ barrier layer.^{58,59}

Studying the catalytic properties of a metal layer would require other considerations. An oxidized B₄C layer with carbon contamination is unlikely to be the ideal substrate for a metal sample layer. Ideally, the sample layer should be deposited right after the multilayer deposition in the same chamber, without intermittent exposure to ambient air. Nonetheless, this alone may not be sufficient to obtain a metallic catalyst layer that would be stable at temperatures of interest. Processes such as de-wetting and diffusion of the surface layer under study through the MLM capping layer (or vice versa) should be examined for each sample configuration. Deposition of adhesion layers might be necessary to prevent

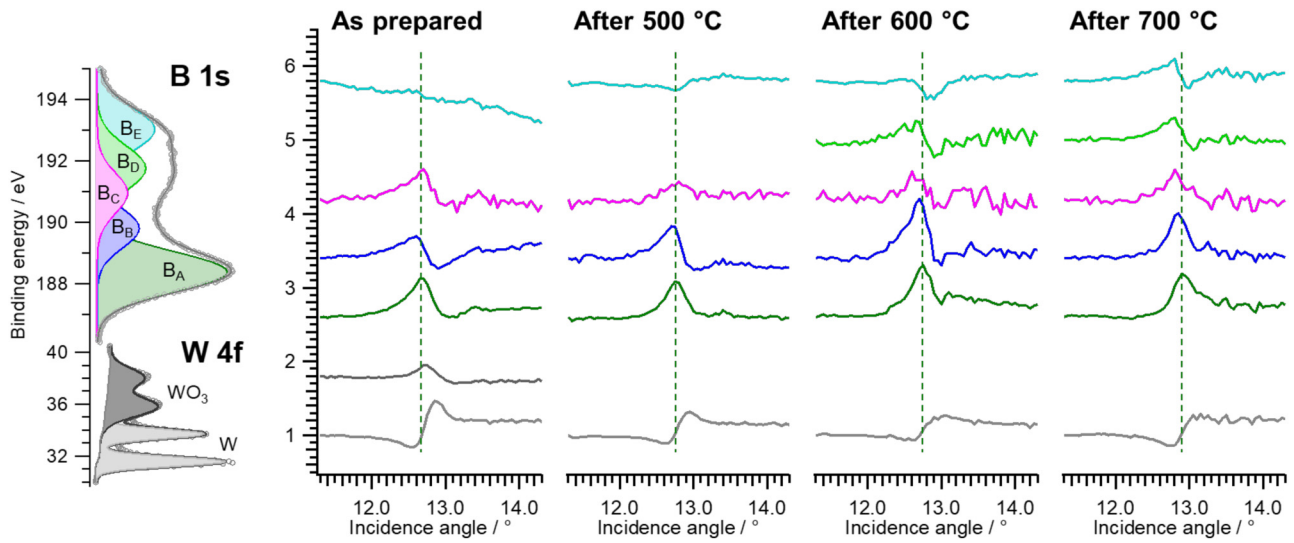


FIG. 9. Rocking curves from B 1s and W 4f photoemission components of the B_4C/W MLM as prepared, and after annealed in UHV at 500, 600, and 700 °C. WO_3 is present only in the as-prepared sample, whereas the B_D component has a significant intensity only after annealing to 600 °C. The peak position of the B_A rocking curve is indicated with a vertical line for reference. Each rocking curve is normalized to the signal at the lowest incidence angle for that rocking curve. All data are plotted with an offset in y for better visibility.

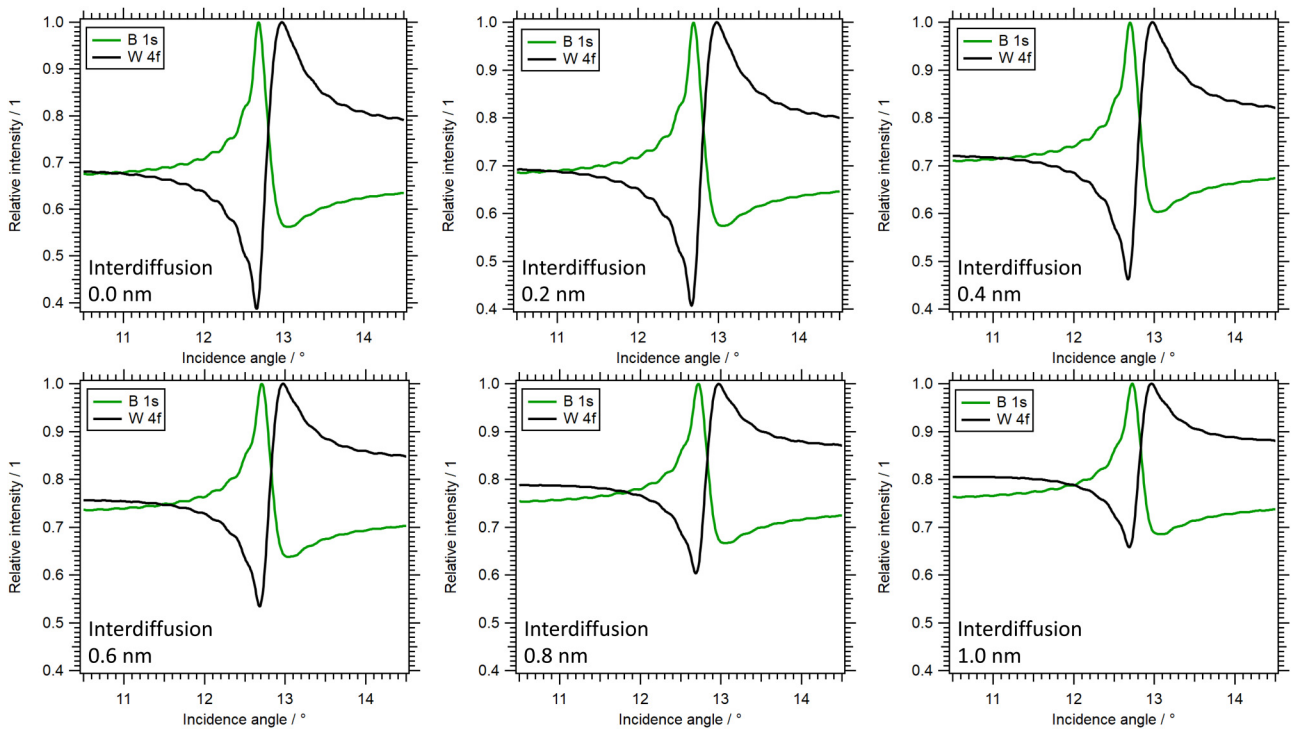


FIG. 10. Calculated rocking curves for total signal of B 1s and W 4f at different degrees of interdiffusion. For details, see text.

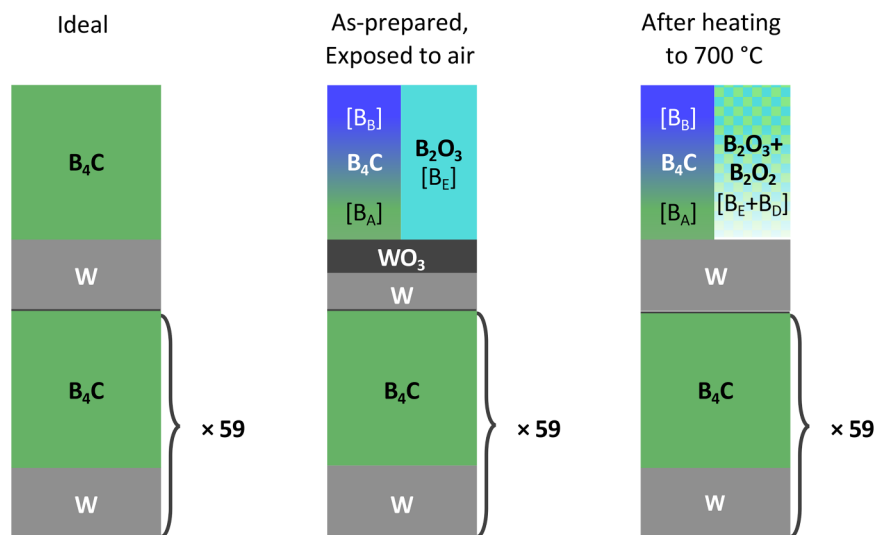


FIG. 11. Schematic representations of the structure of the MLM based on the analysis of the photoemission spectra and the rocking curves. “Ideal,” “as-prepared,” exposed to air,” and “after heating to 700 °C” represent the sample right after preparation, before exposure to air (not-measured); after exposure to air; and after the last annealing step at 700 °C in UHV. The labels in brackets are the assignments for the B 1s peaks based on the fits shown in Fig. 6.

de-wetting, but this could lead to more problems such as contamination of the surface. In any case, well-planned and executed future work would be necessary to tap into the potential of this powerful method for the study of catalytic surfaces.

IV. CONCLUSIONS

A B_4C/W multilayer with B_4C termination was tested for thermal stability in UHV in view of its surface composition and x-ray standing-wave generation characteristics. In the as-prepared state, i.e., after prolonged exposure to air, the top B_4C layer contained about 30% of the B in the form of B_2O_3/H_3BO_3 . Some WO_3 was also observed at the interface between B_4C and W, indicating diffusion of oxygen through the B_4C capping layer. Annealing up to 700 °C in UHV did not lead to any significant change in the total O 1s intensity, but the oxygen redistributed between W and B_4C . Between 400 and 600 °C, WO_3 and B_4C reacted to form more oxidized boron (B^{3+} and B^{2+}). From the data it is not possible to determine if the initially present WO_3 was reduced during the thermal treatment to W metal, a boride, or a carbide, since the W 4f binding energies of all these compounds are similar. Although the O 1s signal decreased at 700 °C, the B 1s signal increased, which suggests that O at the surface diffused into the bulk. The appearance of the B 1s peak at ~ 191.8 eV is related to the formation of B_2O_2 via the reaction of B_2O_3 with B.

Despite the chemical changes, the overall reflectivity and consequently the capability of these MLMs to act as SW generators stayed largely unaffected, as revealed by the rocking curve modulations of the boron species. B_4C/W MLMs are, thus, promising substrates to study catalytic systems at elevated temperatures with high depth precision. The excellent depth selectivity of the SW measurement can be used to specifically investigate surface and/or buried interface(s), relevant for particular catalytic systems. As an outlook, the chemical stability of these MLMs will be studied in different reactive gaseous environments, such as O_2 , CO, and H_2O , while

chemical changes of individual layers can again be monitored using SWAPPS.

ACKNOWLEDGMENTS

The ALS is supported by the Director, Office of Science, Office of Basic Energy Sciences of the U.S. Department of Energy at the Lawrence Berkeley National Laboratory under Contract No. DE-AC02-05CH11231. H.B., O.K., and A.S. acknowledge support by the Director, Office of Science, Office of Basic Energy Sciences, and by the Division of Chemical Sciences, Geosciences, and Biosciences of the U.S. Department of Energy at the Lawrence Berkeley National Laboratory under Contract No. DE-AC02-05CH11231.

DATA AVAILABILITY

The data that support the findings of this study are available from the corresponding authors upon reasonable request.

REFERENCES

- H. R. Pruppacher and J. D. Klett, *Microphysics of Clouds and Precipitation* (Kluwer Academic, Dordrecht, 1979).
- R. Schlögl, *Angew. Chem. Int. Ed.* **42**, 2004 (2003).
- G. E. Brown and G. Calas, *Geochem. Persp.* **1**, 483 (2012).
- E. McCafferty, *Introduction to Corrosion Science* (Springer, New York, 2010).
- A. K. Petford-Long and A. N. Chiamonti, *Ann. Rev. Mat. Res.* **38**, 559 (2008).
- W. Giurlani, E. Berretti, M. Innocenti, and A. Lavacchi, *Coatings* **10**, 1211 (2020).
- D. A. Shapiro *et al.*, *Nat. Photonics* **8**, 765 (2014).
- L. A. Giannuzzia and F. A. Stevie, *Micron* **30**, 197 (1999).
- P. Mondal, P. C. Pradhan, P. Tiwari, and A. K. Srivastava, *AIP Conf. Proc.* **1731**, 060014 (2016).
- G. S. Harlow, E. Lundgren, and M. Escudero-Escribano, *Curr. Opin Electrochem.* **23**, 162 (2020).
- S. Hüfner, *Photoelectron Spectroscopy* (Springer, Berlin, 1995).

- ¹²As an aside we note that XPS can also be used in sputter-depth profiling as probe for the chemical composition in deeper layers into the bulk, albeit in that case in a destructive manner. See, e.g., M. P. Seah, *Vacuum* **34**, 463 (1984).
- ¹³B. Batterman, *Phys. Rev.* **133**, A759 (1964).
- ¹⁴M. J. Bedzyk, D. Bilderback, J. White, H. D. Abrufia, and M. G. Bommaritos, *J. Phys. Chem.* **90**, 4926 (1986).
- ¹⁵P. Fenter, L. Cheng, S. Rihs, M. Machesky, M. J. Bedzyk, and N. C. Sturchio, *J. Colloid Interf. Sci.* **225**, 154 (2000).
- ¹⁶C. S. Fadley, *J. Electron Spectrosc. Relat. Phenom.* **190**, 165 (2013).
- ¹⁷A. X. Gray, *J. Electron Spectrosc. Relat. Phenom.* **195**, 399 (2014).
- ¹⁸H. Siegbahn, *J. Phys. Chem.* **89**, 897 (1985).
- ¹⁹D. F. Ogletree, H. Bluhm, E. L. D. Hebenstreit, and M. Salmeron, *Nucl. Instrum. Methods Phys. Res., Sect. A* **601**, 151 (2009).
- ²⁰D. E. Starr, Z. Liu, M. Hävecker, A. Knop-Gericke, and H. Bluhm, *Chem. Soc. Rev.* **42**, 5833 (2013).
- ²¹J. Schnadt, J. Knudsen, and N. Johansson, *J. Phys.: Condens. Matter* **32**, 413003 (2020).
- ²²C. Arble, M. Jia, and J. T. Newberg, *Surf. Sci. Rep.* **73**, 37 (2018).
- ²³S. Nemsák *et al.*, *Nat. Commun.* **5**, 5441 (2014).
- ²⁴O. Karshoğlu *et al.*, *Faraday Discuss.* **180**, 35 (2015).
- ²⁵A. F. Jankowski, L. R. Schrawyer, and M. A. Wall, *J. Appl. Phys.* **68**, 5162 (1990).
- ²⁶P. Siffalovic *et al.*, *J. Appl. Cryst.* **43**, 1431 (2010).
- ²⁷P. N. Rao, S. K. Rai, M. Nayak, and G. S. Lodha, *Appl. Opt.* **52**, 6126 (2013).
- ²⁸B. Huang, W. Le, Y. Wang, X. Luo, and Y. Yang, *Appl. Surf. Sci.* **464**, 10 (2019).
- ²⁹P. S. Singam, M. Nayak, R. Gupta, P. C. Pradhan, A. Majhi, S. Narendranath, and P. Sreekumar, *J. Astronom. Telesc. Instrum. Syst.* **4**, 044003 (2018).
- ³⁰H. Bluhm *et al.*, *J. Electr. Spectrosc. Rel. Phenom.* **150**, 86 (2006).
- ³¹S. Tanuma, C. J. Powell, and D. R. Penn, *Surf. Interface Anal.* **21**, 165 (1994).
- ³²Kolibrik.net, s.r.o—KolXPd, see: <https://www.kolibrik.net/kolxpd/>.
- ³³S.-H. Yang, A. X. Gray, A. M. Kaiser, B. S. Mun, B. C. Sell, J. B. Kortright, and C. S. Fadley, *J. Appl. Phys.* **113**, 073513 (2013).
- ³⁴I. Jiménez, D. G. J. Sutherland, T. van Buuren, J. A. Carlisle, L. J. Terminello, and F. J. Himpsel, *Phys. Rev. B* **57**, 13167 (1998).
- ³⁵S.-H. Yang, B. S. Mun, A. W. Kay, S.-K. Kim, J. B. Kortright, J. H. Underwood, Z. Hussain, and C. S. Fadley, *Surf. Sci.* **461**, L557 (2000).
- ³⁶S.-H. Yang, B. S. Mun, A. W. Kay, S.-K. Kim, J. B. Kortright, J. H. Underwood, Z. Hussain, and C. S. Fadley, *J. Electron Spectrosc. Rel. Phenom.* **114**, 1089 (2001).
- ³⁷J. F. Moulder and J. Chastain, *Handbook of X-ray Photoelectron Spectroscopy A Reference Book of Standard Spectra for Identification and Interpretation of XPS Data* (Physical Electronics Division, Perkin-Elmer Corporation, Eden Prairie, MN, 1992).
- ³⁸D. N. Hendrickson, J. M. Hollander, and W. L. Jolly, *Inorg. Chem.* **9**, 612 (1970).
- ³⁹W. E. Moddeman, A. R. Burke, W. C. Bowling, and D. S. Foose, *Surf. Interface Anal.* **14**, 224 (1989).
- ⁴⁰W. C. Foo, J. S. Ozcomert, and M. Trenary, *Surf. Sci.* **255**, 245 (1991).
- ⁴¹C. W. Ong and H. Huang, *J. Appl. Phys.* **95**, 3527 (2004).
- ⁴²D. J. Joyner and D. M. Hercules, *J. Chem. Phys.* **72**, 1095 (1980).
- ⁴³Y. J. Wang, J. F. Fan, and M. Trenary, *Chem. Mater.* **5**, 192 (1993).
- ⁴⁴V. I. Nefedov, *X-ray Electron Spectroscopy of Chemical Compounds* (Khimiya, Moscow, 1984).
- ⁴⁵S. Balci, N. A. Sezgi, and E. Eren, *Ind. Eng. Chem. Res.* **51**, 11091 (2012).
- ⁴⁶Y. J. Wang and M. Trenary, *Surf. Sci. Spectra* **1**, 183 (1992).
- ⁴⁷Y. J. Wang and M. Trenary, *Chem. Mater.* **5**, 199 (1993).
- ⁴⁸R. J. Colton and J. W. Rabalais, *Inorg. Chem.* **15**, 236 (1976).
- ⁴⁹M. Belyansky, M. Trenary, and C. Ellison, *Surf. Sci. Spectra* **3**, 147 (1994).
- ⁵⁰T. S. Moss, *Proc. Phys. Soc. London, Sect. A* **64**, 590 (1951).
- ⁵¹J. Lagrenaudie, *J. Phys. Radium* **13**, 554 (1952).
- ⁵²J. Lagrenaudie, *J. Phys. Radium* **14**, 14 (1953).
- ⁵³E. S. Greiner and J. A. Gutowski, *J. Appl. Phys.* **28**, 1364 (1957).
- ⁵⁴W. C. Shaw, D. E. Hudson, and G. C. Danielson, *Phys. Rev.* **107**, 419 (1957).
- ⁵⁵F. H. Horn, *J. Appl. Phys.* **30**, 1611 (1959).
- ⁵⁶F. H. Horn, *J. Appl. Phys.* **30**, 1612 (1959).
- ⁵⁷C. B. Hood and M. O. Thurston, *J. Electrochem. Soc.* **109**, 66 (1962).
- ⁵⁸X. Song, E. Primorac, H. Kühlenbeck, and H.-J. Freund, *J. Phys. Chem. C* **120**, 8185 (2016).
- ⁵⁹X. Song, E. Primorac, H. Kühlenbeck, and H.-J. Freund, *Surf. Sci.* **653**, 181 (2016).